Transition moments beyond the electric-dipole approximation: Visualization and basis set requirements

Martin van Horn, Nanna Holmgaard List, Trond Saue

Transition Moments Beyond the Electric-Dipole Approximation: Visualization and Basis Set Requirements

Martin van Horn,[1, a)] Nanna Holmgaard List,[2, b)] and Trond Saue[1, c)]

[1)] *Laboratoire de Chimie et Physique Quantiques, UMR 5626 CNRS — Université Toulouse III-Paul Sabatier, 118 route de Narbonne, F-31062 Toulouse, France.*

[2)] *Department of Chemistry, School of Engineering Sciences in Chemistry, Biotechnology and Health (CBH), KTH Royal Institute of Technology, SE-10044 Stockholm, Sweden.*

(Dated: 14 November 2023)

In the simulation of X-ray absorption spectroscopy, the validity of the electric-dipole approximation comes into question. Three different schemes exist to go beyond this approximation: the first scheme is based on the full semi-classical light–matter interaction, whereas the latter two schemes, referred to as the generalized length and velocity representation, are based on truncated multipole expansions. Even though these schemes have been successfully implemented in several quantum chemistry codes, their basis set requirements remained largely unknown. Here, we assess the basis set requirements of these three schemes. We have considered the $1s_{1/2}$ and $7s_{1/2} \rightarrow 7p_{1/2}$ transitions in the radium atom, representative of core and valence excitations, respectively, and have carried out calculations with the dyall.aeXz (X=2,3,4) basis sets at the four-component relativistic TD-HF level of theory. Our basis set study was greatly factilitated by the generation and visualization of radial distributions of the transition moment densities, allowing straightforward comparison with equivalent finite-difference calculations. Pertaining to the truncated interaction, we find that the length representation electric multipoles is the easiest to converge, requiring the dyall.ae2z basis for low-order multipoles and the dyall.ae4z basis at higher orders. The magnetic multipole moments follow a similar trend, although they are more difficult to converge. The velocity representation electric multipoles are the most difficult to converge: at high orders, the dyall.ae3z and dyall.ae4z basis sets introduce artificial peaks and oscillations, which increase the overall error. These artifacts are associated with linear dependence issues in the small component space of the larger basis sets. The full interaction operator, however, does not suffer from these problems, and we therefore recommend its use in the simulation of x-ray spectroscopy.

Keywords: light–matter interactions beyond the electric-dipole approximation, basis set requirements, X-ray spectroscopy, four-component relativistic framework

[a)] Electronic mail: mvanhorn@irsamc.ups-tlse.fr

[b)] Electronic mail: nalist@kth.se

[c)] Electronic mail: trond.saue@irsamc.ups-tlse.fr

I. INTRODUCTION

Recent developments of high-brilliance synchrotron radiation have opened up a window of possibilities for X-ray absorption spectroscopy (XAS).[1,2] XAS is a term used to describe two different spectroscopic techniques: X-ray absorption fine structure (XAFS), either near-edge (NEXAFS) or extended (EXAFS). The former describes excitations close to the ionization threshold, whereas the latter gathers information from electrons that are scattered by high energy photons.[3,4] Due to the high energies involved in the experiment, these techniques probe electrons that are buried deep inside the core. Since core orbitals tend to be localized around the nuclei, XAS provide site- and element-specific information about the system under consideration.[5] Even though much useful information can be extracted from experiment alone, assignment and interpretation of these spectra require input from theory and simulation. Therefore, the advances in experimental techniques should go hand-in-hand with the development of theory and implementations thereof.

To properly simulate XAS, it is necessary to include several effects beyond what is typically required for UV-Vis spectroscopy. First of all, since relativistic effects are generated in the core region, they need consideration in the simulation of core excitations already for quite light elements.[6,7] Secondly, after exciting the core electron, the system is left with a core-hole that reduces the screening of the nuclear charge. As a result, the effective nuclear charge increases, which amounts to an additional stabilization of the excited state, referred to as core-hole relaxation.[8,9] Third, the spatial variations of the short wavelength X-rays may induce multipole transitions, suggesting that proper models should incorporate effects beyond the electric-dipole approximation to explain all observed peaks. To simulate these effects, various bodies of theory need to be applied, each having distinct basis set requirements. In contemporary scientific literature, a plethora of recommendations is available for basis sets designed for the description of relativistic effects[10–12] and core-hole relaxation.[13–17] On the contrary, the available literature that assesses the basis set requirements of non-dipolar effects in spectroscopic calculations is limited.[18,19]

In our previous work, we have presented three schemes to simulate semi-classical light–matter interaction beyond the electric-dipole approximation. The first scheme is based on the full light–matter interaction, implying that the interaction operator retains the same sinusoidal form as the electromagnetic fields from which it is derived. This was initially

implemented in a non-relativistic framework[20,21] and then more recently extended to the 4-component (4c) relativistic level.[22,23] Facilitated by the additional simplifications provided by the relativistic framework, we were able to realize two further schemes based on truncated interaction, along the lines of Bernadotte *et al.*,[24] but in our case to *arbitrary* order in the wave vector. We have also extended these schemes to the simulation of electronic circular dichroism.[23] Recently, Foglia and co-workers reported the use of the full light–matter interaction in the simulation of both electronic and magnetic circular dichroism.[25]

In the complete basis set limit, our two schemes based on a truncated interaction, referred to as the generalized length and velocity representation, yield equivalent oscillator strengths. We stress that these two approaches should be applied with caution, as they may introduce slow convergence of the multipole expansion as well as gauge-origin dependence.[22] Bernadotte and coworkers found a remedy to the latter problem: they demonstrated that oscillator strengths in the velocity representation is formally origin-independent for each order in terms of the wave vector.[24] We have shown, though, that origin-independence may be broken for large displacements as a result of numerical issues.[22] The length representation, on the other hand, is inherently dependent on the choice of expansion point, as we have pointed out in previous work.[22] Besides these complications, the basis set requirements of the aforementioned schemes need to be assessed in order to validate the performance of the basis sets used in former and any future work.

Conventional basis sets are constructed by choosing a set of functions that minimize the energy. Typically, more energy is gained by adding tight functions than diffuse functions.[26] Because of this, energy-optimized basis sets saturate the core region faster than the tail-region. The full and truncated light–matter interaction may require addition of further basis functions. A problem in this respect is the lack of a variational principle for transition moments. Alternatively, basis sets for use beyond energies can be constructed using the equivalent core approximation,[27,28] Slater's rule[17,29] or the completeness-optimization scheme.[30,31] Another strategy is to systematically increase the basis set size, until the property of interest has become stable.

Sørensen *et al.* performed such a series in a non-relativistic framework using the full and truncated interaction operator, the latter limited to second order, expressed with the ANO-RCC basis sets.[18,19] Even though the series did not fully converge for the larger basis sets, their results indicated that the full interaction operator is more stable with respect to

basis set choice. In addition, Sørensen *et al.* argued that each multipole moment requires different basis sets, making it exceedingly difficult to construct basis sets that can describe the truncated interaction at higher orders. They concluded that the full interaction operator should be the standard for calculations involving non-dipolar effects. For zeroth- and first-order interactions, the length representation seems to be the preferred choice in the literature, although there is not a concise answer as to which representation has a superior basis set convergence.[32–35]

Another strategy to gauge the quality of a basis set is to compare with a reference value. In the present work, the basis set requirements for non-dipolar effects are assessed by comparing calculations using Gaussian basis sets and the molecular code DIRAC[36] to equivalent finite-difference calculations using the atomic code GRASP.[37] Specifically, we investigate the basis set convergence of the transition moments in the three abovementioned schemes. To this end, we have chosen to study the $1s_{1/2} \rightarrow 7p_{1/2}$ and the $7s_{1/2} \rightarrow 7p_{1/2}$ transitions in the radium atom, representative of core and valence excitations, respectively. Since the $s_{1/2}$ and $p_{1/2}$ orbitals in the finite basis approximation are constructed exclusively from s- and p-exponents, the basis set considerations boil down to finding what additional diffuse or tight functions are required to converge intensities. In general, diffuse and tight functions improve the description of the outer and inner regions of the wave function. To examine which regions need improvement, we visualize the transition moment densities (that is, the densities that integrate to the transition moments) as radial distributions. This also allows straightforward comparison of calculations using different basis sets, all the way to the complete basis set limit, effectively provided by the finite-difference calculations. To the best of our knowledge our use of radial distributions is a novel approach that may also find use for other properties. While the basis set convergence obtained for the radium atom may not be completely transferable to the molecular domain, we believe that these results can serve as general guidelines for choosing a suitable basis set.

This work is organized as follows: first, we provide the necessary theory for setting up the model system; followed by a description of the computational details used to perform the calculations on this model; then the results of these tests will be presented and discussed.

II. THEORY

In this Section we briefly summarize our three schemes for the calculation of intensities using full and truncated light–matter interaction. We also explain the calculation of transition moments within the linear reponse regime. Finally, for our model system, we give explicit expressions for the radial distributions of the relevant transition moment densities in terms of radial functions. The latter already gives some hints about basis set requirements.

A. Full and truncated light–matter interaction

We have previously presented three different schemes to describe linear absorption of linear and circularly polarized light beyond the electric-dipole approximation.[22,23] To take the effects of relativity into account, all three schemes are based on the Dirac Hamiltonian

$$\hat{h} = c(\boldsymbol{\alpha} \cdot \mathbf{p}) + \beta mc^2 + ec(\boldsymbol{\alpha} \cdot \mathbf{A}) - e\phi, \tag{1}$$

where $(\boldsymbol{\alpha}, \beta)$ are the Dirac matrices and $(\mathbf{A}, \phi)$ the electromagnetic potentials. Unlike its non-relativistic counterpart, the Dirac Hamiltonian is linear, and not quadratic, in the vector potential, which greatly simplifies the formalism.

The first scheme relies on the full interaction operator, giving rise to the following oscillator strength between initial and final states, $|i\rangle$ and $|f\rangle$, respectively

$$f_{fi} = \frac{2\omega_{fi}}{\hbar e^2} \left| \langle f | \hat{T}(\omega_{fi}) | i \rangle \right|^2; \quad \hat{T}(\omega) = \frac{e}{\omega} (c\boldsymbol{\alpha} \cdot \boldsymbol{\epsilon}) e^{i\mathbf{k}\cdot\mathbf{r}} \tag{2}$$

where $-e$ is the electron charge and $\hbar$ the reduced Planck constant. The incident electromagnetic wave is represented by the frequency ω, the polarization vector $\boldsymbol{\epsilon}$ and the wave vector $\mathbf{k}$ of length $k = \frac{\omega}{c}$. In this way, all non-dipolar effects are included, but it comes at a somewhat higher computational cost because the integrals gain frequency-dependency and the expression for isotropic averaging is carried out on a Lebedev grid.[21] However, we have reduced these costs significantly by efficient code-design and parallelization.

The alternative method is to expand the oscillator strength in orders of the wave vector[24] and truncate it at a finite order

$$f_{fi}^{[2n]} = \frac{2\omega_{fi}}{\hbar e^2} \sum_{m=0}^{n} (2 - \delta_{m0}) \epsilon_p \epsilon_q k_{j_1} k_{j_2} \dots k_{j_{2n}} \mathrm{Re} \left\{ \langle f | \hat{X}^{[n+m]}_{j_1 \dots j_{n+m};p}(\omega_{fi}) | i \rangle \langle f | \hat{X}^{[n-m]}_{j_{n+m+1} \dots j_{2n};q}(\omega_{fi}) | i \rangle^* \right\}, \tag{3}$$

where the nth-order multipole operators

$$\hat{X}^{[n]}_{j_1\ldots j_n;p}(\omega) = \frac{1}{(n+1)!}\hat{Q}^{[n+1]}_{j_1\ldots j_n;p} - \frac{i}{\omega}\frac{1}{n!}\hat{m}^{[n]}_{j_1\ldots j_{n-1};r}\varepsilon_{rj_np} \tag{4}$$

are decomposed into an electric and magnetic component, respectively. In this expression, the Einstein summation convention has been applied. Note that the truncated oscillator strength only appears at even orders, as can be shown by considerations of time-reversal symmetry.[22] Furthermore, the multipole operator can be expressed in two forms: the generalized length and velocity representations.

The generalized length representation can be derived by imposing multipolar gauge, giving rise to Cartesian multipole moments in their conventional form

$$\begin{aligned} \hat{Q}^{[n+1]}_{j_1\ldots j_np} &= -er_{j_1}\ldots r_{j_n}r_p \\ \hat{m}^{[n]}_{j_1\ldots j_{n-1};r} &= \frac{n}{n+1}r_{j_1}\ldots r_{j_{n-1}}(\mathbf{r}\times\hat{\mathbf{j}})_r; \quad \hat{\mathbf{j}} = -ec\boldsymbol{\alpha}. \end{aligned} \tag{5}$$

Alternatively, the full interaction, Eq. (2), can be Taylor-expanded with respect to the wave vector,

$$\hat{T}(\omega) = \sum_{n=0}^{\infty} i^{n-1}\hat{T}^{[n]}; \quad \hat{T}^{[n]} = \frac{e}{\omega}\frac{1}{n!}(ic\boldsymbol{\alpha}\cdot\boldsymbol{\epsilon})(\mathbf{k}\cdot\mathbf{r})^n, \tag{6}$$

which results in the generalized velocity representation. In this form, the generalized velocity representation does not distinguish between electric and magnetic multipole moments. However, as we have shown in previous works,[22,23] it is possible to rework, using vector algebra, the above operator in a form that makes such a separation. The electric multipole operators in the generalized velocity representation then read

$$\hat{\mathcal{Q}}^{[n+1]}_{j_1\ldots j_n;p} = \frac{ie}{\omega}r_{j_1}\ldots r_{j_{n-1}}(c\alpha_p r_{j_n} + nc\alpha_{j_n}r_p), \tag{7}$$

whereas the magnetic multipole moments are the same as in the generalized length representation. Hereafter, the generalized length and velocity representation electric multipoles will be designated as the electric-length and electric-velocity multipoles. The seemingly different expressions for the electric multipole moment operators are related through

$$\frac{1}{\omega_{fi}}\langle f|\left[\hat{h}, \epsilon_p k_{j_1}\ldots k_{j_n}\hat{Q}^{[n+1]}_{j_1\ldots j_np}\right]|i\rangle = \langle f|\epsilon_p k_{j_1}\ldots k_{j_n}\hat{\mathcal{Q}}^{[n+1]}_{j_1\ldots j_n;p}|i\rangle. \tag{8}$$

In the above form, this relation only applies under exact-state conditions. However, with an alternative approach we show, in Section S2, the equivalence of electric-length and electric-

velocity multipoles in the complete basis set limit at the Hartree–Fock level of theory. Previously, such equivalence has been shown between electric-*dipole* length and velocity representations for Hartree–Fock.[38–40] For extensions to the (non-hybrid) Kohn–Sham and MCSCF case, the reader may consult Refs. 41 and 42, respectively.

B. Radial transition moment distributions

In order to construct transition moments, as for instance in Eq. (2), formally three components are required: the initial state, the interaction operator ($\hat{\Omega}$) and the final state. The initial state is given by the ground state, which will be approximated by the Hartree–Fock determinant ($|\Phi_0\rangle$). Furthermore, the transition moments will be derived from the four types of interaction operators introduced in Eqs. (2), (5) and (7). In the following, they are labeled by Ω-subscripts (T: full, Q: electric-length:, M: magnetic and $\mathcal{Q}$: electric-velocity). It thus remains to find an expression for the final state. However, explicit construction of this state can be avoided by applying linear response theory: it is known that excitation energies and transition moments can be extracted from the poles and residues of linear response functions.[42–44] This amounts to solving the following generalized eigenvalue equation

$$E_0^{[2]}\mathbf{X} = \hbar\omega S^{[2]}\mathbf{X}. \tag{9}$$

From the structure of the electronic Hessian $E_0^{[2]}$ and the generalized metric $S^{[2]}$

$$E_0^{[2]} = \begin{pmatrix} A & B \\ B^* & A^* \end{pmatrix}; \quad S^{[2]} = \begin{pmatrix} \Sigma & \Delta \\ -\Delta^* & -\Sigma^* \end{pmatrix}, \tag{10}$$

it can be shown that solution vectors come in pairs

$$\left\{ \omega_+ = +\left|\omega_{fi}\right|, \mathbf{X}_+ = \begin{pmatrix} \boldsymbol{Z} \\ \boldsymbol{Y}^* \end{pmatrix} \right\} \bigcup \left\{ \omega_- = -\left|\omega_{fi}\right|, \mathbf{X}_- = \begin{pmatrix} \boldsymbol{Y} \\ \boldsymbol{Z}^* \end{pmatrix} \right\}. \tag{11}$$

Transition moments can be obtained by contracting the solution vectors with the property gradient. At the self-consistent field (SCF) level of theory, the property gradient is given by

$$\mathbf{E}_\Omega^{[1]} = \begin{pmatrix} \boldsymbol{g}_\Omega \\ \boldsymbol{g}_\Omega^* \end{pmatrix}; \quad g_{\Omega;ai} = \langle\Phi_0|\big[-\hat{a}_i^\dagger\hat{a}_a, \hat{\Omega}\big]|\Phi_0\rangle, \tag{12}$$

where the elements of the property gradient are expressed in second quantization with i and a referring to occupied and virtual orbitals, respectively. Therefore, at the linear response level of theory, transition moments can be expressed as

$$\langle f|\hat{\Omega}|i\rangle^{LR} = \mathbf{X}_+^\dagger \mathbf{E}_\Omega^{[1]} = \sum_{ai} \left[Z_{ai}^* \langle \Phi_i^a|\hat{\Omega}|\Phi_0\rangle + Y_{ai} \langle \Phi_0|\hat{\Omega}|\Phi_i^a\rangle \right]. \tag{13}$$

Such transition moments, obtained within the finite-basis approximation, are to be compared with equivalent quantities obtained from a numerical atomic code that exploits the form

$$\phi_{n\kappa m}(\mathbf{r}) = \frac{1}{r} \begin{pmatrix} P_{n\kappa}(r)\xi_{\kappa m}(\theta,\phi) \\ iQ_{n\kappa}(r)\xi_{-\kappa m}(\theta,\phi) \end{pmatrix}, \tag{14}$$

of 4-component relativistic atomic orbitals.[45] The angular part is given by spherical spinors, $\xi_{\kappa,m}(\theta,\phi)$, which depend on the angular quantum numbers κ and m. The radial functions, $P_{n\kappa}(r)$ and $Q_{n\kappa}(r)$ depend on n and κ, but, contrary to the one-electron case, the label n is in the many-electron case a counting index rather than the principal quantum number. For the non-relativistic hydrogen atom, n indicates the number of radial nodes through the relation[46]

$$N_{nodes} = n - \ell - 1, \tag{15}$$

where ℓ represents the orbital angular momentum quantum number. To the authors' knowledge, there is no exact relativistic extension to this rule, although it has been observed empirically that $P_{n\kappa}$ contains the same number of nodes as the non-relativistic radial wave function.[47,48] On the other hand, the difference in radial nodes between the large and small component has been worked out exactly.[47] For negative values of κ, both components have the same number of radial nodes, whereas the small component has one additional node for positive κ. Here we would like to add that in Ref. 45, the relation $N_{nodes} = n - |\kappa|$ is used to count radial nodes of the large component. However, we have confirmed with analytic calculations that this relation does not give the right number of nodes.

The radial functions $P(r)$ and $Q(r)$ are obtained by solving the radial equations for each occupied orbital self-consistently on a grid. Inserting the orbitals from Eq. (14) into the transition moments thus enables us to compare basis set calculations with a numerical reference. For these purposes, the transition moments can be expressed conveniently in

terms of radial distributions

$$R_\Omega(r) = \int_0^{2\pi} d\phi \int_0^{\pi} d\theta \; r^2 \sin\theta \; \Omega_{fi}(\mathbf{r}); \quad \Omega_{fi}(\mathbf{r}) = \phi^\dagger_{n_i,\kappa_i,m_i}(\mathbf{r})\hat{\Omega}\phi_{n_f,\kappa_f,m_f}(\mathbf{r}) \tag{16}$$

where $\Omega_{fi}(\mathbf{r})$ is the density that integrates to the transition moment, T_Ω. The quality of a basis set can be assessed by looking at the deviations of the basis set distributions with respect to the reference distribution.

The alert reader may note that in the above expression the transition moment is given by a single term, whereas in the linear response expression, Eq. (13), there are two terms, corresponding to contributions from resonant excitation amplitudes and their anti-resonant de-excitation partners. Part of the answer is that in exact-state and also CI response theory the B block of the Hessian, Eq. (10), coupling excitations and de-excitations, is zero, whereas this is not the case in HF response theory (setting it to zero constitutes the Tamm–Dancoff approximation[49]); in all three cases the corresponding Δ-block of the generalized metric is zero. A more complete discussion on this point is found in Section S1.

In the present work we investigate radial transition moment distributions of $n_i s_{1/2} \rightarrow 7p_{1/2}, (n_i = 1, 7)$ excitations of the radium atom, with $\Omega = T, Q, m, \mathcal{Q}$. From parity it follows that only odd electric and even magnetic multipoles contribute. We have chosen a frame in which the wave vector $\mathbf{k}$ is aligned with the z-axis and the polarization vector $\boldsymbol{\epsilon}$ with the y-axis. The radial distribution for the electric-length multipoles then becomes

$$R_Q^{[2n+1]}(r) = \frac{e r^{2n+1}}{(2n+1)(2n+3)}(P_{7,1}P_{n_i,-1} + Q_{7,1}Q_{n_i,-1}), \tag{17}$$

the electric-velocity

$$R_{\mathcal{Q}}^{[2n+1]}(r) = \frac{-ecr^{2n}}{\omega(2n+1)(2n+3)}\left((2n-1)P_{7,1}Q_{n_i,-1} - (2n+3)Q_{7,1}P_{n_i,-1}\right) \tag{18}$$

and the magnetic multipole distribution

$$R_M^{[2n]} = \frac{iec2n(2n-1)r^{2n+1}}{\sqrt{2}(2n+1)^2(2n+3)}\left(P_{7,1}Q_{n_i,-1} + Q_{7,1}P_{n_i,-1}\right), \tag{19}$$

where the r-dependence of the radial functions P and Q have been suppressed. The radial distribution associated with the full interaction reads

$$R_T(r) = \frac{iec}{3\omega}\Big(\big(j_0(kr) - j_2(kr)\big)P_{7,1}Q_{n_i,-1} + 3j_0(kr)Q_{7,1}P_{n_i,-1}\Big), \tag{20}$$

where $j_0(kr)$ and $j_2(kr)$ are the zeroth and second order spherical Bessel functions, given by

$$j_0(kr) = \frac{\sin kr}{kr}; \quad j_2(kr) = \left(\frac{3}{(kr)^2} - \frac{1}{kr}\right)\sin kr - \frac{3}{(kr)^2}\cos kr. \tag{21}$$

The spherical Bessel functions appear in these expression as a consequence of the plane wave expansion

$$e^{i\mathbf{k}\cdot\mathbf{r}} = 4\pi \sum_{\ell=0}^{\infty}\sum_{m=-\ell}^{\ell} i^{\ell} j_{\ell}(kr) Y_{\ell}^{m}(\mathbf{e}_k) Y_{\ell}^{m*}(\mathbf{e}_r). \tag{22}$$

In this expansion, Y_{ℓ}^{m} represents a spherical harmonic, while $\mathbf{e}_k$ and $\mathbf{e}_r$ represent the wave and radial unit vectors, respectively. For small values of kr, the limiting forms of the spherical Bessel functions are[50]

$$\lim_{kr\to 0} j_{\ell}(kr) \sim \frac{(kr)^{\ell}}{(2\ell+1)!!}. \tag{23}$$

This relation implies that all Bessel functions except j_0 are zero at the origin. We can use this result to obtain

$$\lim_{kr\to 0} R_T(r) = \frac{iec}{3\omega}\left(P_{7,1}Q_{n_i,-1} + 3Q_{7,1}P_{n_i,-1}\right) = iR_{\mathcal{Q}}^{[1]}(r). \tag{24}$$

Therefore, the electric-dipole approximation is correctly retrieved in the long wavelength limit of Eq. (20).

Without performing any calculations, the shape of Eqs. (17)–(20) already tells us useful information about the basis set requirements of the interaction operators. For example, the radial distributions corresponding to the multipole moments (Eqs. (17)–(19)) all contain a prefactor depending on a power of the radial distance. This prefactor is in competition with the terms associated with the atomic radial functions: the former tends towards infinity for large distances, whereas the latter decays to zero. Because the atomic functions decay exponentially, the transition moments are finite. From these considerations it follows that the multipole moments with increasing order sample regions farther and farther away from the nucleus and thus we expect that they may require additional diffuse functions for their proper description. This is in sharp contrast with the full interaction, Eq. (20). Instead of the radial powers, this distribution depends on the spherical Bessel functions, which assume the following asymptotic form[50]

$$\lim_{kr\to\infty} j_{\ell}(kr) \sim (kr)^{-1}\sin(kr - \frac{1}{2}\ell\pi). \tag{25}$$

Therefore, the spherical Bessel functions decay to zero for $kr \to \infty$, which implies that the radial distribution of the full interaction will decay much faster than the multipole distributions. Consequently, the full interaction is expected to require fewer diffuse basis functions than the multipole moment operators.

III. COMPUTATIONAL DETAILS

To compare basis set effects in both the valence and core regions, we considered the $7s_{1/2} \to 7p_{1/2}$ and the $1s_{1/2} \to 7p_{1/2}$ transition of the radium atom. The transitions were constrained to occur between single orbitals to facilitate the comparison between the Gaussian-type-orbital calculations in DIRAC[36,51] and the numerical reference calculations in GRASP.[37] Since GRASP only computes *occupied* orbitals, we decided to optimize orbitals, using average-of-configurations (AOC) Hartree–Fock,[52] with respect to *excited-state* determinants, i.e., $[\mathrm{Rn}]7s^1_{1/2}7p^1_{1/2}$ for the valence transition and $[\mathrm{Ra}]1s^{-1}_{1/2}7p^1_{1/2}$ for the core transition. Even though the $7p_{1/2}$ orbital is formally occupied in these configurations, we treat it as a virtual orbital to construct transition moments. In the case of GRASP these were obtained by inserting the $P_{n\kappa}$ and $Q_{n\kappa}$ radial functions into Eqs. (17)–(20). Since transition moments are only determined up to a complex phase, we defined them such that all radial distributions are real and have a positive maximum value. Since the radial functions from GRASP are calculated on a numerical grid and thus effectively correspond to the complete basis set limit, the GRASP transition moments were used as reference. In the case of DIRAC, we applied overlap selection to prevent the core-excited state to collapse during the SCF cycles.[53–55] We then used the orbitals of the excited state calculations in a ground state four-component time-dependent Hartree–Fock (4c-TD-HF) calculation within the linear response regime.[44] The restricted excitation window method[56,57] was invoked to only consider one amplitude in Eq. (13). The radial distributions were then divided by this remaining amplitude to compare the results of the basis set calculations with the numerical reference values. In DIRAC the radial distributions were calculated on a radial grid with the visualization module, which performs the angular integration on a Lebedev grid ($L_{\mathrm{max}} = 64$). Due to the quaternion symmetry scheme[58] in DIRAC, all transition moments are real by default. Further details on this are provided in the Supplementary Material.

The basis set calculations were carried out at the Hartree–Fock level of theory using the

Dirac–Coulomb Hamiltonian and the dyall.aeXz (X=2,3,4) basis sets.[59,60] These basis sets are constructed from uncontracted Cartesian Gaussian basis functions which are designed for correlated calculations and hence contain basis functions of high orbital angular momentum. We trimmed off the g, h and i functions because for atomic systems they will only contribute to the space of virtual orbitals. The small component basis sets were generated according to the condition of restricted kinetic balance[10,61–63] and the $(SS|SS)$ integrals were treated exactly, for consistency with the numerical calculations. Furthermore, we found that with the default linear dependence threshold (10^{-6} and 10^{-8} for the large and small component space, respectively), several basis functions were deleted. Especially the small component of the $1s_{1/2}$ was susceptible to the deletion of functions. This deteriorates the quality of the results, so for all calculations, the linear dependence threshold was set to 10^{-9} and 10^{-10} for the large and small component space, respectively. In Section S3, the problems associated with linear dependence are further discussed.

IV. RESULTS AND DISCUSSION

We start by comparing the radial distributions of the core and valence excitations within the electric-dipole approximation (velocity representation; Figure 1). To illustrate their radial extent, the expectation value of the radial distance for different s orbitals are indicated. A striking observation is that the radial distribution for the core transition is much more localized around the nucleus than that of the valence transition. This follows from the locality of the core orbital. Furthermore, the valence distribution oscillates considerably more than the core distribution, and one can see that the oscillations follow the shell structure of the atom. The electric transition dipole distribution is stable with respect to the choice of basis set, since all basis set calculations overlap with the numerical reference. The relative deviations (depicted in the right corner of Figure 1) further confirm this. Therefore, for both transitions, the dyall.ae2z basis set is sufficient to properly describe electric transition dipole moments.

To gauge the importance of non-dipolar effects, the electric-velocity dipole distributions are compared to those of the full interaction in Figure 2. The basis set convergence of the full interaction appears to be similar as the electric-dipole moment, since the full interaction is unaffected by the choice of basis set. For the valence transition, the electric-dipole

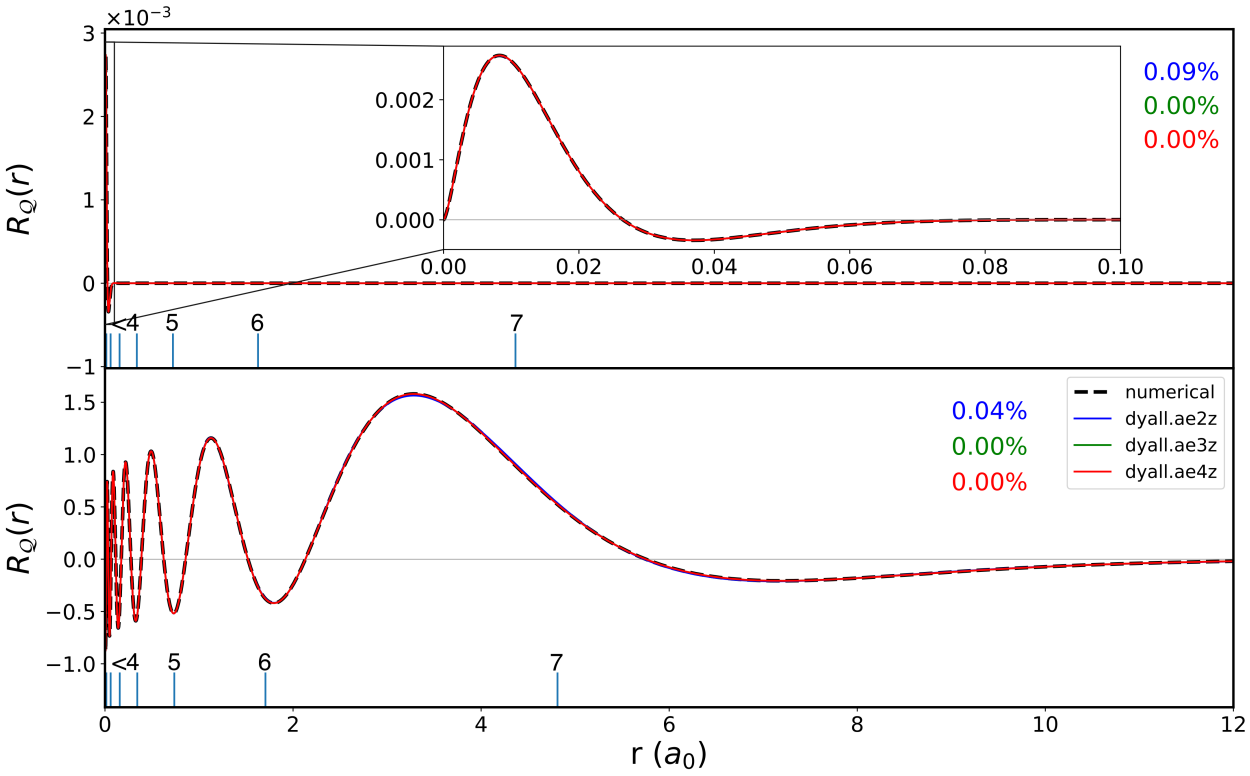

FIG. 1. Radial distribution of the electric-velocity dipole moment ($R_Q^{[1]}$) for the $1s_{1/2}$ (top panel) and $7s_{1/2} \rightarrow 7p_{1/2}$ (bottom panel) transitions. Expectation values of the radial position for the relevant s orbitals are indicated as vertical sticks where the labels represent the index of the s orbital, i.e. $n_i s_{1/2}$ ($n_i = 1, \ldots, 7$). The percentages in the upper right corner of each box are the relative errors of the transition moments, i.e. $|\frac{T_{bas}-T_{num}}{T_{num}}|\times 100\%$.

distributions basically coincide with the full interaction, which confirms the validity of the electric-dipole approximation in this energy regime. Even, for the core transition, the difference between the distributions of the electric-dipole and full interaction is modest. The electric-dipole approximation breaks down if the wavelength of the electromagnetic field is small compared to the spatial extent of the transition. Though the wavelength for the core transition falls in the hard X-ray regime, the compactness of the radium $1s_{1/2}$ orbital reduces the importance of non-dipolar effects. It remains an open question, however, whether non-dipolar effects play a more important role in extended systems.[20]

The oscillatory behavior in Figures 1 and 2, or the lack thereof, can be understood by considering the radial part of the atomic orbitals involved in the core and valence transition (Figures 3 and 4, respectively). Note that the $7p_{1/2}$ orbitals are, as expected, not identical for

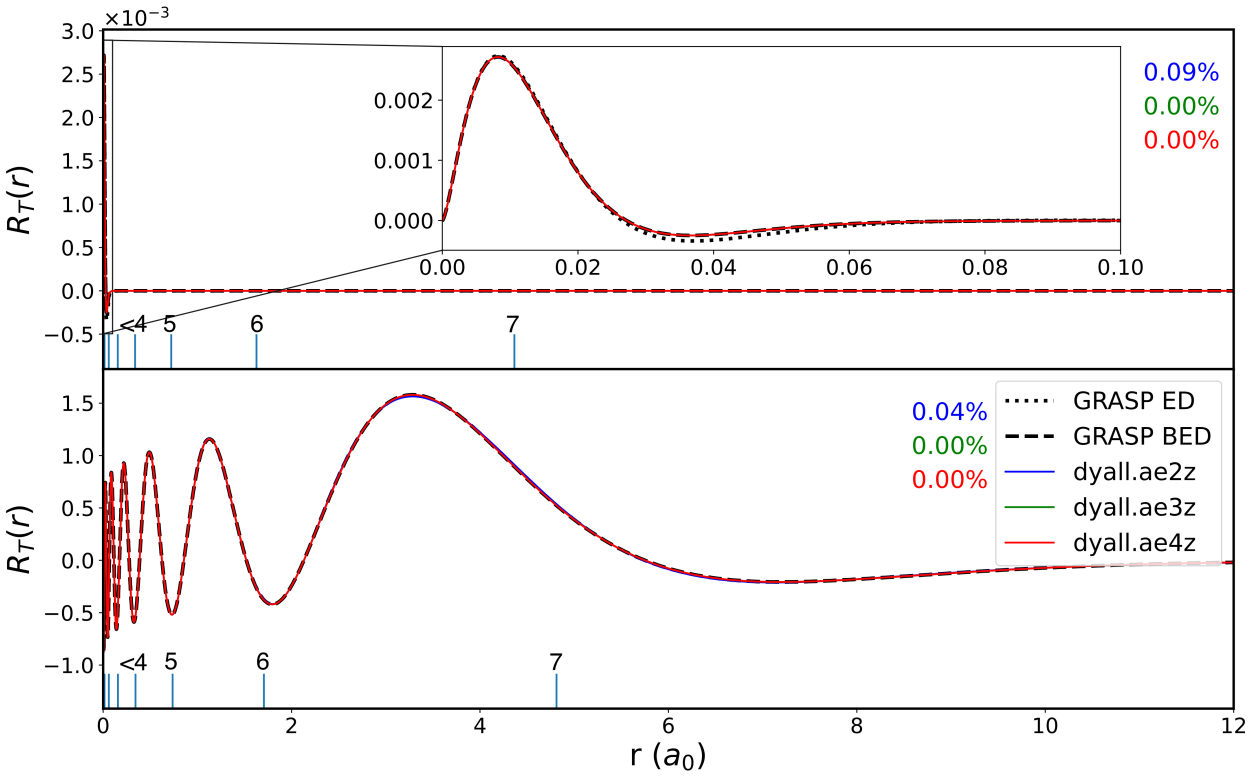

FIG. 2. Radial distribution of the full interaction (R_T) for the $1s_{1/2}$ (top panel) and $7s_{1/2} \rightarrow 7p_{1/2}$ (bottom panel) transitions. To assess the validity of the electric-dipole approximation, the numerical reference curve from the full interaction (GRASP BED) is compared with the reference curve from the electric-velocity dipole (GRASP ED). Expectation values of the radial position are shown for the relevant s orbitals. The labels represent the index of the s orbital, i.e. $n_i s_{1/2}$ ($n_i = 1, \ldots, 7$). The percentages in the upper right corner of each box are the relative errors of the transition moments, i.e. $|\frac{T_{bas}-T_{num}}{T_{num}}|\times 100\%$.

the two transitions, since the orbitals have been optimized in different excited configurations. Because the number of radial nodes is not easily observed from these figures, we have plotted each orbital separately with bigger margins and determined the number of nodes by visual inspection. Using this method, we found that the number of radial nodes follows the rules prescribed in the theory section. For all orbitals, the basis set calculations nearly coincide with the numerical reference, which makes it difficult to assess the performance of each basis set. Therefore, we need to analyze the error curves in Figures 3 and 4 to properly assess the basis set convergence. From the analytical formulas in Eqs. (17)-(19), we expect that the basis set error is most relevant at large radial distances. For that reason, we will

investigate the error at much larger distances than the range of the radial functions (bottom row subfigures).

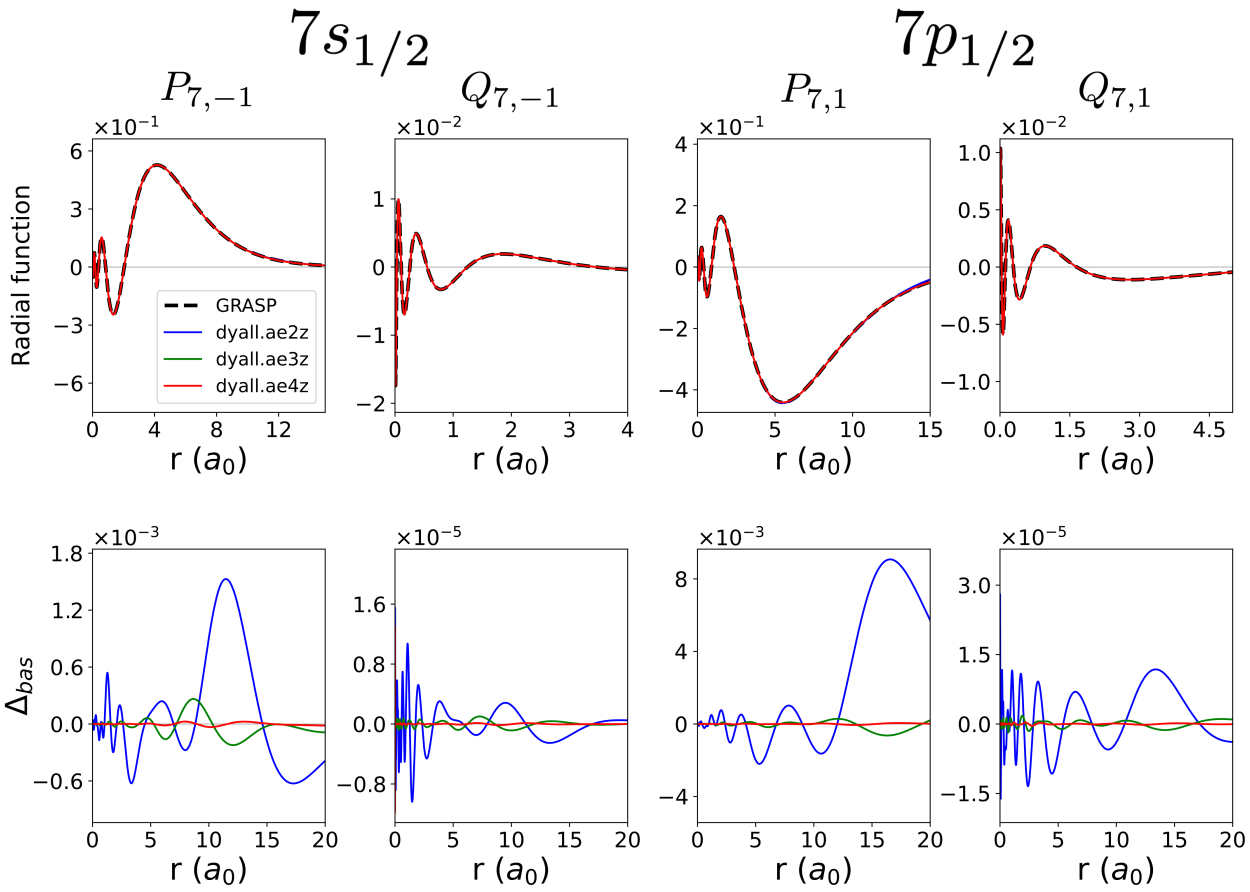

FIG. 3. Radial functions of the large and small component of the $7s_{1/2}$ ($\langle r \rangle = 4.365\ a_0$) and $7p_{1/2}$ orbital (top row) and their deviations from the numerical reference (bottom row). These orbitals were taken from the radium atom with [Rn]$7s^1_{1/2}7p^1_{1/2}$ configuration. The basis set orbitals were calculated at the 4c-HF level using DIRAC, while the numerical reference was calculated with GRASP. Note that the scaling is different for each individual box and that the error curves are plotted in a different range than the radial functions.

To some extent, all error curves in these plots are oscillatory, reflecting the incompleteness of the basis set. In general, the amplitude of the oscillations diminish with larger basis sets, although the frequency increases. This trend can clearly be observed in Figures 3 and 4: the small error associated with the dyall.ae2z basis is even further reduced by using the dyall.ae3z basis set, at the expense of a higher frequency of the oscillations, while the dyall.ae4z set flattens most of the error curves. However, the additional improvement introduced by the

dyall.ae4z basis set is marginal for the $Q_{1,-1}$ function, and the dyall.ae4z curve seems to oscillate more compared to the dyall.ae3z curve.

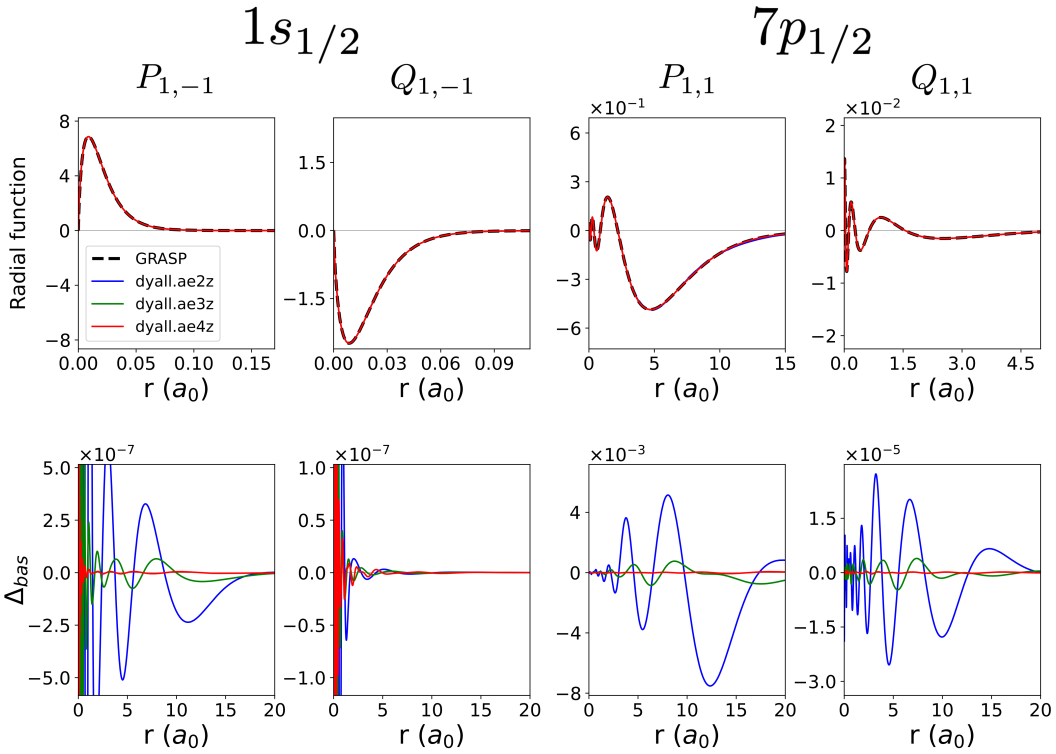

FIG. 4. Radial functions of the large and small component of the $1s_{1/2}$ ($\langle r \rangle = 0.01454\, a_0$) and $7p_{1/2}$ orbital (top row) and their deviations from the numerical reference (bottom row). These orbitals were taken from the radium atom with $[\mathrm{Ra}]1s^{-1}_{1/2}7p^{1}_{1/2}$ configuration. The basis set orbitals were calculated at the 4c-HF level using DIRAC, while the numerical reference was calculated with GRASP. Note that the scaling is different for each individual box and that the error curves are plotted in a different range than the radial functions.

It has proven to be challenging to completely eliminate the error of the $Q_{1,-1}$ function, as it is highly susceptible to problems associated with linear dependence. As explained in Section S3, the use of scalar basis functions in DIRAC may accentuate such problems. By increasing the linear dependence threshold, we could significantly reduce the deviations from the reference, although the basis set convergence of the $Q_{1,-1}$ function is still not completely smooth. The minute differences between numerical and basis set orbitals suggest the radial distributions of the multipole moments should be stable across basis sets series.

In practice, this is, however, not completely true. Figures 5 and 6 depict the radial distributions of the electric-length multipoles, $\hat{Q}^{[2n+1]}$, for the valence and core transitions, respectively. In both figures, the peak of the reference curve appears close to the origin and moves farther away at higher orders. Additionally, the peak height and the integrated value of these curves seems to rise upon increase of the order. The same trend can be observed in the error curves, which are most pronounced in the regions far from the nucleus. In the following, we will define an error below 1% as acceptable convergence. Therefore, the dyall.ae2z basis set is an acceptable choice for multipole moments below order 2. For $2 < n < 5$, the dyall.ae3z is needed to reduce the error below 1%. Even with the largest basis set, the accuracy goal is not reached for the highest two orders. These trends are even more pronounced in the case of the core transition (Figure 6). For this transition, the largest dyall.ae4z basis set is already needed at $n > 3$. In general, the overall error increases with the order of the multipole moments. These findings can be understood by considering the form of the the radial distribution in Eq. (17). The multiplication by the power of the radial distance of increasing orders blows up the moderate deviations in radial densities (Figures 3 and 4).

Figure 7 contains the radial distributions of the magnetic multipole moments $\hat{m}^{[2n]}$ for the valence transition. For the lowest two orders, these distributions have distinct shapes, whereas their shapes start to be reminiscent of the electric multipole distributions in Figures 5 and 6 for higher orders. Likewise, the peaks of the radial distributions move away from the origin and become higher upon increasing the order. The overall errors indicate that the dyall.ae3z basis set is preferable for $2 < n < 5$, whereas the dyall.ae4z basis set should be used at higher orders. However, for $n = 6$ and $n = 7$, the dyall.ae4z basis does not reduce the overall error below 1%. The magnetic multipole moments for the core transition (Figure 8) follow the same trend, although the higher order multipole moments tend to converge with more difficulties towards the numerical reference. Already at $n = 4$, the dyall.ae4z basis set is not enough to reduce the error below 1%. In general, the basis set convergence of the magnetic multipole moments seem to follow the same trends as the electric-length multipole moments, although the convergence of the former is much more demanding. Furthermore, note that the dyall.ae4z curve has two peaks for $n = 5$, whereas the reference curve only contains one peak.

Similar artifacts arise in the radial distributions of the electric-velocity multipole moments

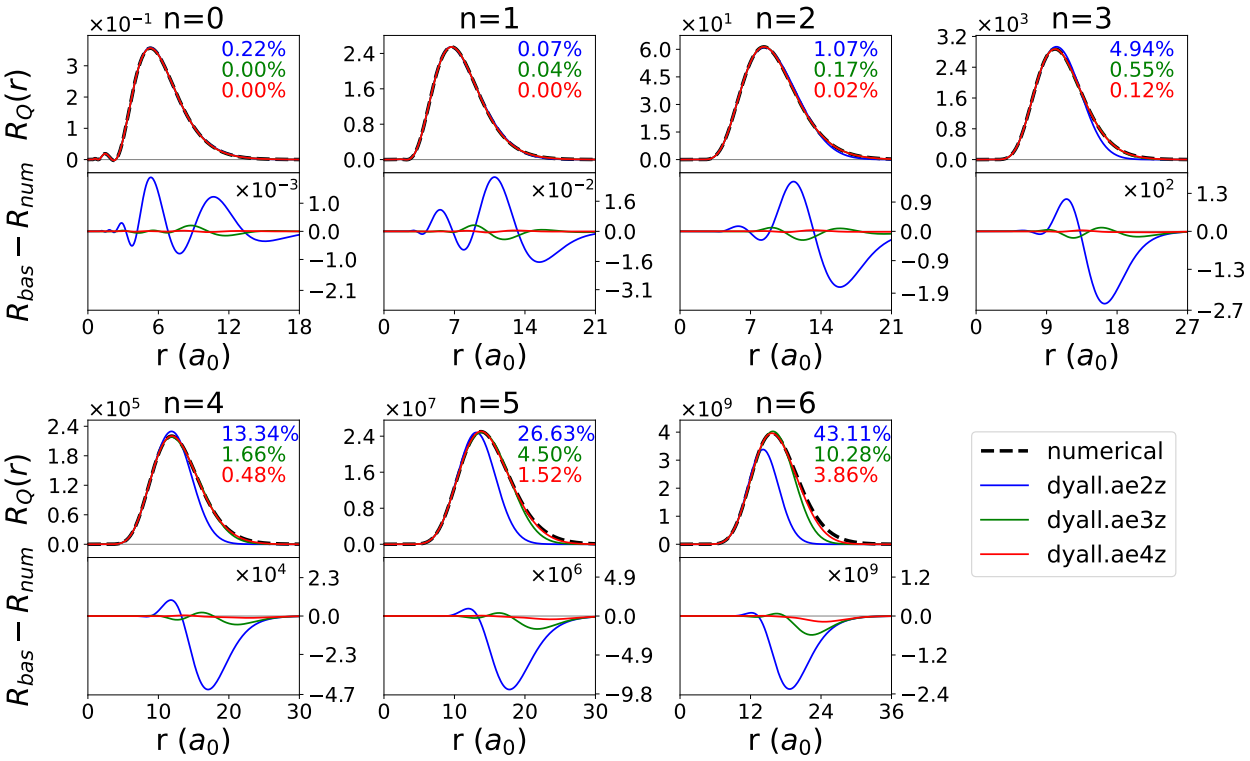

FIG. 5. Valence transition ($7s_{1/2} \rightarrow 7p_{1/2}$): radial distributions of electric multipole moments in the generalized length representation, $\hat{Q}^{[2n+1]}, n \in [0, 6]$. In each box, the upper panel contains the radial distribution, while the lower panel contains the deviation with the numerical reference. Note that each subfigure has different scales. The percentages in the upper right corner of each box are the relative errors of the transition moments, i.e. $|\frac{T_{\text{bas}} - T_{\text{num}}}{T_{\text{num}}}| \times 100\%$.

$\hat{\mathcal{Q}}^{[2n+1]}$ (Figures 9 and 10 for valence and core transitions, respectively). In both cases, the reference curve follows the same pattern as the other multipole moment. For the valence transition, the dyall.ae2z basis set is sufficient to converge the lowest three orders, whereas the dyall.ae3z basis set should be used at higher orders. For the core transition, the radial distributions are extremely problematic to converge. At $n > 3$ the dyall.ae4z is still not enough to converge towards the reference. Furthermore, at these orders, the dyall.ae4z curves contain additional peaks that are not present in the reference curves. Due to these artifacts, the overall error for $n > 4$ follows a counter-intuitive trend: the dyall.ae2z basis set performs better then the larger bases.

Interestingly, the artificial peaks only appear for the magnetic and electric-velocity distributions, whereas the electric-length distributions converge smoothly towards the numerical

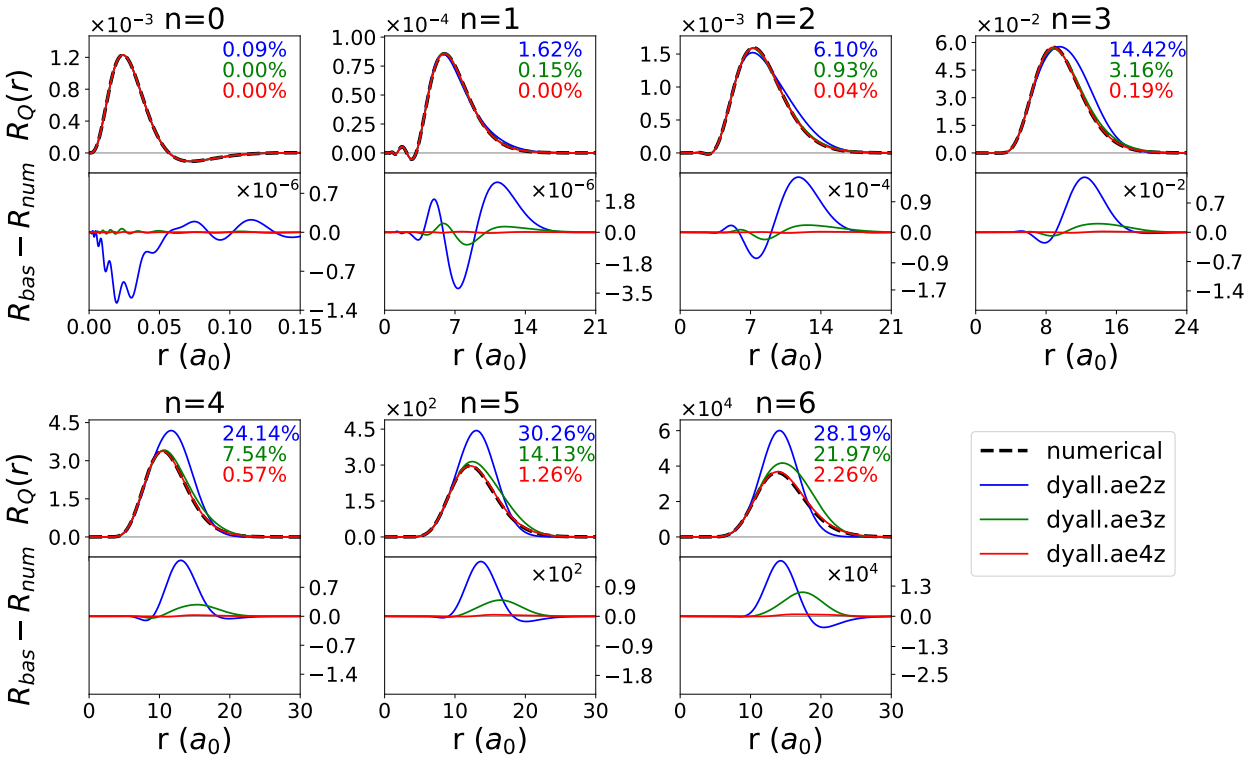

FIG. 6. Core transition ($1s_{1/2} \rightarrow 7p_{1/2}$): radial distributions of electric multipole moments in the generalized length representation, $\hat{Q}^{[2n+1]}, n \in [0, 6]$. In each box, the upper panel contains the radial distribution, while the lower panel contains the deviation with the numerical reference. Note that each box has a different scale. The percentages in the upper right corner of each box are the relative errors of the transition moments, i.e.$|\frac{T_{\mathrm{bas}} - T_{\mathrm{num}}}{T_{\mathrm{num}}}| \times 100\%$.

reference. This observation can be understood from the problematic basis set convergence of the $Q_{1,-1}$ function (Figure 4). After all, the magnetic and electric-velocity distributions depend on the $\boldsymbol{\alpha}$-matrices, which couple the small and large components, whereas the electric-length distribution is diagonal in these two components (see for example Eqs. (17)–(20)). In Figure 4, we have observed that the larger basis sets introduce small oscillations in the error curve of the $Q_{1,-1}$ function. These oscillations in the electric-length multipoles are contained in the small–small contribution to the transition density and are thus comparatively small. For the two other types of multipole moments, the oscillations reside in the large–small contribution and are amplified at large distances by the power of the radial distance, thus creating the artificial peaks in Figures 8 and 10. Similar artifacts are avoided when applying the full interaction operator. As can be inferred from Eq. (20), the error as-

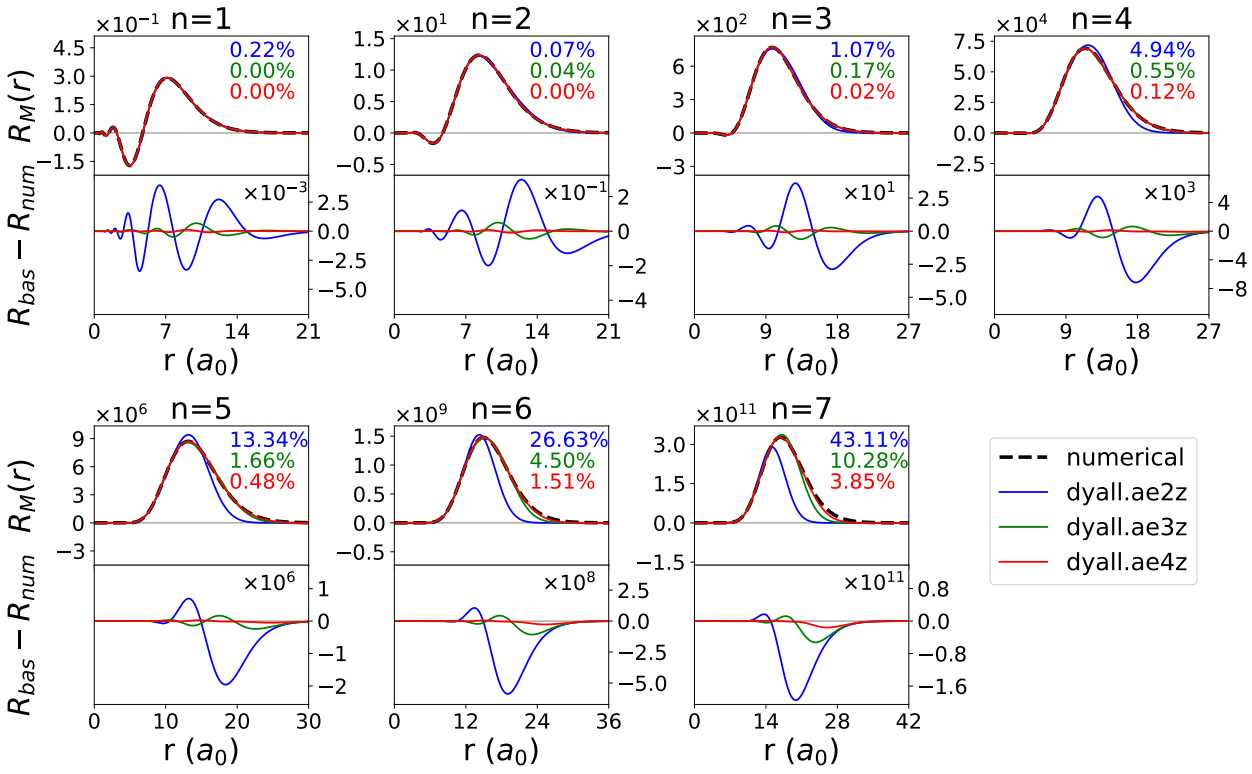

FIG. 7. Valence transition ($7s_{1/2} \rightarrow 7p_{1/2}$): radial distributions of magnetic multipole moments $\hat{m}^{[2n]}, n \in [1, 7]$. In each box, the upper panel contains the radial distribution, while the lower panel contains the deviation with the numerical reference. Note that each box has a different scale. The percentages in the upper right corner of each box are the relative errors of the transition moments, i.e. $|\frac{T_{\mathrm{bas}} - T_{\mathrm{num}}}{T_{\mathrm{num}}}| \times 100\%$.

sociated with the tail region of the orbitals is not blown out of proportion when applying the full interaction operator. Consequently, this renders the full interaction stable with respect to basis set choice, essentially being converged already with dyall.ae2z.

Conversely, for the core transition, the low-order multipole moments require the dyall.ae3z basis set to obtain reasonable accuracy, whereas even the dyall.ae4z basis set is not enough for the highest orders. However, it might be possible that similar accuracy can be achieved with smaller basis sets. Compared to the dyall.ae2z, the dyall.ae4z basis set contains additional tight functions and high-angular momentum functions that might be irrelevant for the construction of multipole moments. We attempted to augment the dyall.ae2z basis set in an even-tempered fashion with diffuse functions to obtain a better balance between computational costs and performance, but all of these basis sets introduced unphysical oscillations, as

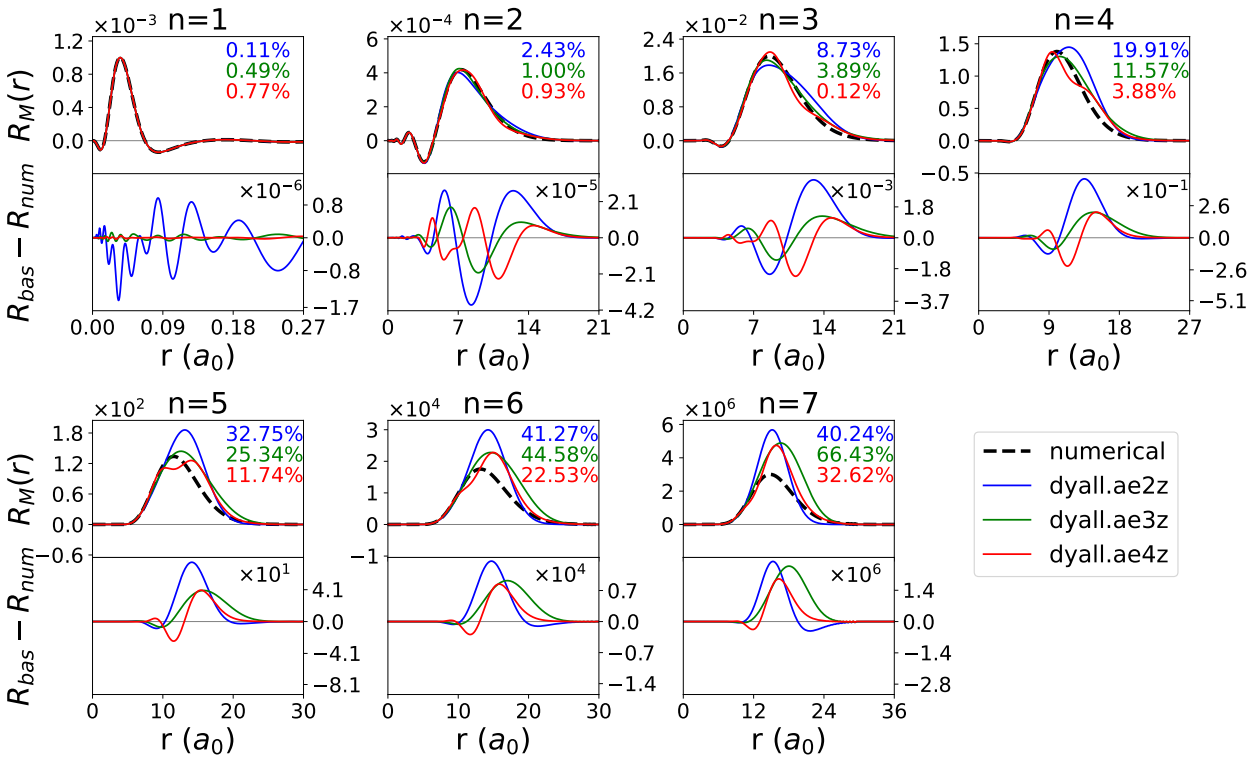

FIG. 8. Core transition ($1s_{1/2} \rightarrow 7p_{1/2}$): radial distributions of magnetic multipole moments $\hat{m}^{[2n]}, n \in [1, 7]$. In each box, the upper panel contains the radial distribution, while the lower panel contains the deviation with the numerical reference. Note that each box has different scales. The percentages in the upper right corner of each box are the relative errors of the transition moments, i.e. $|\frac{T_{\text{bas}} - T_{\text{num}}}{T_{\text{num}}}| \times 100\%$.

shown in Section S4. Alternatively, a smaller basis could be constructed by applying a similar scheme as Jensen and coworkers.[14] They augmented the cc-pVnZ basis set with the core polarization functions of the cc-pCV(n+1)Z basis set. We tried a similar procedure to add diffuse functions to the dyall.ae2z basis, but this also led to unphysical oscillations. These findings suggest that the improved convergence observed with increased cardinal number X of the dyall.aeXz series is not only due to the increased range of exponents, but also their distribution within that range.

What remains is to apply the basis sets to the calculation of oscillator strengths. By inspection of Figures 5–10, it seems that the value of the transition moments become increasingly larger at higher orders, suggesting that the oscillator strengths of both the valence and core transitions have convergence problems with respect to the multipole expansion. To

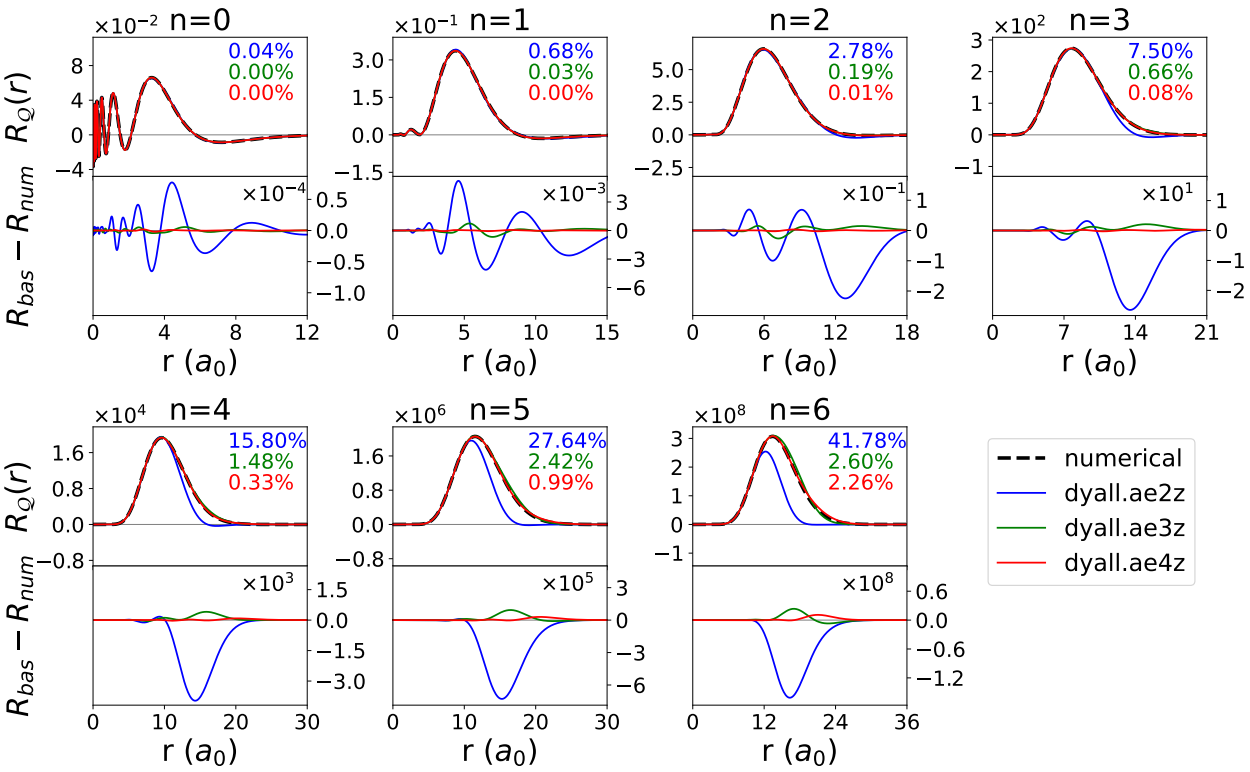

FIG. 9. Valence transition ($7s_{1/2} \rightarrow 7p_{1/2}$): radial distributions of electric multipole moments in the generalized velocity representation $\hat{\mathcal{Q}}^{[2n+1]}, n \in [0, 6]$. In each box, the upper panel contains the radial distribution, while the lower panel contains the deviation with the numerical reference. Note that each box has a different scale. The percentages in the upper right corner of each box are the relative errors of the transition moments, i.e. $|\frac{T_{\rm bas} - T_{\rm num}}{T_{\rm num}}| \times 100\%$.

validate this proposition, we report the anisotropic oscillator strengths for the single orbital $1s_{1/2}$ and $7s_{1/2} \rightarrow 7p_{1/2}$ transitions for both the full and truncated interactions in Table I. However, upon inspection of the values in Table I, it becomes clear that the multipole expansion already converges at zeroth order for the valence transition. This appears to be in contradiction with the steady growth of transition moments seen in Figures 5, 7 and 9. This can be understood from the damping of the transition moments by increasing powers of the wave vector k, Eq. (3). This is not the case for the $1s_{1/2} \rightarrow 7p_{1/2}$ transition. The oscillator strength corresponding to this transition seems to diverge at higher orders. In fact, we found in our previous work that the multipole expansion converges extremely slowly at higher excitation energies ($\omega = c$ ($\sim$3728 eV)).[22] The basis set series from Table I follows the same trends as the radial distributions.

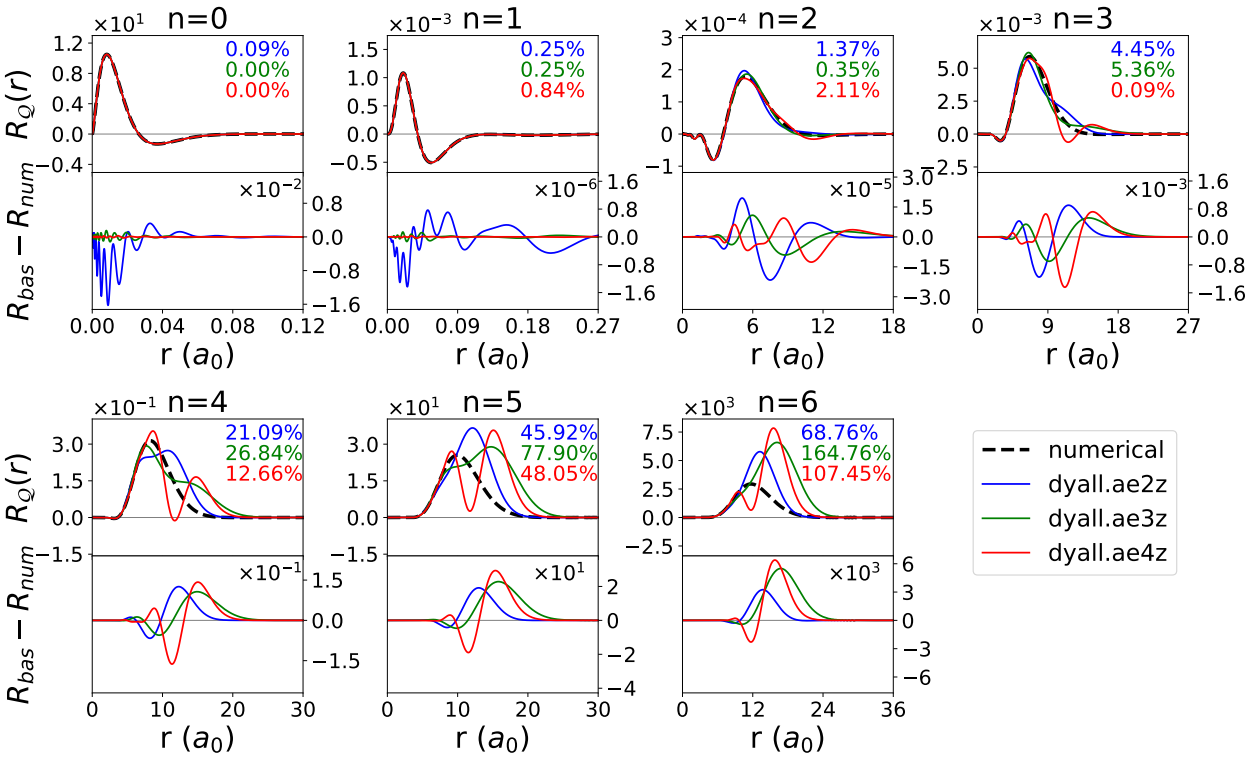

FIG. 10. Core transition ($1s_{1/2} \rightarrow 7p_{1/2}$): radial distributions of electric multipole moments in the generalized velocity representation $\hat{\mathcal{Q}}^{[2n+1]}, n \in [0, 6]$. In each box, the upper panel contains the radial distribution, while the lower panel contains the deviation with the numerical reference. Note that each box has different scales. The percentages in the upper right corner of each box are the relative errors of the transition moments, i.e. $|\frac{T_{\rm bas} - T_{\rm num}}{T_{\rm num}}| \times 100\%$.

A striking observation in Table I is that even with the largest basis set the oscillator strengths in the length- and velocity representation differ by orders of magnitude for both core and valence transitions. More precisely, the ratio lr:vr at zeroth order in k (electric-dipole approximation) is about 0.09 for the valence transition and 8.10 for the core transition, clearly in favor of the latter (vr) when comparing with the full interaction. However, before drawing conclusions on the relative merits of these two representations, one should keep in mind that we show in the Supporting Material that one can only expect equivalence between these two representations when three conditions are met: i) complete basis set limit, ii) variational conditions satisfied and iii) no restrictions on the excitation window. None of these conditions are met for the results presented in Table I. In fact, in order to compare directly with the GRASP reference we have imposed a severely restricted excitation

window and we are using orbitals of a singly-excited state and not the ground state. We will now investigate what happens when we successively comply with conditions iii) and ii).

In Table II we show results obtained after lifting restrictions on the virtual orbital space. We have maintained the restrictions on the occupied space. For the core excitation this is mandatory to assure convergence to the right excitation, and for the valence excitation we find that it is in any case completely dominated by excitation of the $7s_{1/2}$ orbital. For the valence transition, comparison with Table I shows that the oscillator strength using the full interaction is significantly reduced. Its value is very well reproduced within the dipole-velocity representation, whereas the discrepancy with the dipole-length representation increases dramatically. For the core excitation there is, on the other hand, only moderate change with respect to Table I. It is only when we in addition use the proper ground-state orbitals that the dipole-length and dipole-velocity oscillator strengths come into agreement (Table III).

TABLE I. Anisotropic oscillator oscillator strengths ($\frac{c}{\omega}\mathbf{k} = \mathbf{e}_z; \epsilon = \mathbf{e}_y$) of the $ns_{1/2} \rightarrow 7p_{1/2}$ $(n = 1, 7)$ transitions for the full semi-classical interaction operator and accumulated to various orders in the truncated interaction, as indicated by the superscripted numbers in parenthesis, within the multipolar gauge (lr: length representation) and Coulomb gauge (vr: velocity representation), computed at the 4c-TD-HF level of theory with different basis sets. Numbers in parentheses are exponents of 10.

Basis	ΔE (eV)	f_{full}	gauge	$f^{(\rightarrow 0)}$	$f^{(\rightarrow 2)}$	$f^{(\rightarrow 4)}$	$f^{(\rightarrow 6)}$	$f^{(\rightarrow 8)}$	$f^{(\rightarrow 10)}$	$f^{(\rightarrow 12)}$
				$7s_{1/2} \rightarrow 7p_{1/2}$						
dyall.ae2z	1.141	2.603	lr	2.356(-1)	2.356(-1)	2.356(-1)	2.356(-1)	2.356(-1)	2.356(-1)	2.356(-1)
			vr	2.603	2.603	2.603	2.603	2.603	2.603	2.603
dyall.ae3z	1.138	2.605	lr	2.341(-1)	2.341(-1)	2.341(-1)	2.341(-1)	2.341(-1)	2.341(-1)	2.341(-1)
			vr	2.605	2.605	2.605	2.605	2.605	2.605	2.605
dyall.ae4z	1.138	2.605	lr	2.342(-1)	2.342(-1)	2.342(-1)	2.342(-1)	2.342(-1)	2.342(-1)	2.342(-1)
			vr	2.605	2.605	2.605	2.605	2.605	2.605	2.605
				$1s_{1/2} \rightarrow 7p_{1/2}$						
dyall.ae2z	104444.343	1.662(-5)	lr	1.178(-4)	-1.461(-1)	1.806(2)	-1.964(5)	1.954(8)	-1.805(11)	1.556(14)
			vr	1.453(-5)	2.091(-5)	-1.210(-2)	2.072(1)	-2.582(4)	2.689(7)	-2.425(10)
dyall.ae3z	104444.304	1.665(-5)	lr	1.176(-4)	-1.439(-1)	1.726(2)	-1.799(5)	1.723(8)	-1.556(11)	1.346(14)
			vr	1.456(-5)	2.093(-5)	-1.188(-2)	1.974(1)	-2.397(4)	2.531(7)	-2.469(10)
dyall.ae4z	104444.301	1.665(-5)	lr	1.176(-4)	-1.437(-1)	1.713(2)	-1.762(5)	1.649(8)	-1.444(11)	1.203(14)
			vr	1.456(-5)	2.093(-5)	-1.180(-2)	1.926(1)	-2.262(4)	2.291(7)	-2.131(10)

TABLE II. Anisotropic oscillator oscillator strengths ($\frac{c}{\omega}\mathbf{k} = \mathbf{e}_z; \epsilon = \mathbf{e}_y$) of the $ns_{1/2} \rightarrow 7p_{1/2}$ $(n = 1, 7)$ transitions for the full semi-classical interaction operator and the dipole-length and velocity oscillator strengths, calculated with excited state orbitals and no restrictions on the space of virtual orbitals, within the multipolar gauge (lr: length representation) and Coulomb gauge (vr: velocity representation), computed at the 4c-TD-HF level of theory with different basis sets. Numbers in parentheses are exponents of 10.

Basis	ΔE (eV)	f_{full}	$f_{\text{lr}}^{(\rightarrow 0)}$	$f_{\text{vr}}^{(\rightarrow 0)}$	ratio (lr:vr)
		$7s_{1/2} \rightarrow 7p_{1/2}$			
dyall.ae2z	0.146	5.288(-2)	1.421(-4)	5.288(-2)	2.688(-3)
dyall.ae3z	0.113	8.558(-2)	8.554(-5)	8.558(-2)	9.996(-4)
dyall.ae4z	0.111	8.778(-2)	8.218(-5)	8.778(-2)	9.362(-4)
		$1s_{1/2} \rightarrow 7p_{1/2}$			
dyall.ae2z	104444.343	1.568(-5)	1.132(-4)	1.358(-5)	8.336
dyall.ae3z	104444.303	1.571(-5)	1.130(-4)	1.361(-5)	8.306
dyall.ae4z	104444.301	1.571(-5)	1.130(-4)	1.361(-5)	8.306

V. CONCLUSION

We have assessed the basis set requirements for 4c-TD-HF linear absorption calculations with the full semi-classical light-matter interaction operator as well as the truncated interactions in the generalized length and velocity representations. To simplify the basis set considerations, we focused our attention on the underlying transition moments for the $7s_{1/2} \rightarrow 7p_{1/2}$ and the $1s_{1/2} \rightarrow 7p_{1/2}$ transition in the radium atom. We considered the relativistic dyall.aeXz basis set with cardinal numbers X=2,3,4 and compared to a numerical reference. The comparison was facilitated by the generation and visualization of radial distributions of the corresponding transition moment densities, an approach that we believe is unique to the present work.

To lowest orders, the dyall.ae2z basis set was sufficient to converge the length representation electric multipole moments for both transitions. At higher orders, the dyall.ae4z basis was needed. It was commonly observed that the core transition tends to be more difficult to converge than the valence transition. The basis set convergence of the magnetic multipole moments follows these trends as well, although it seems to be even more difficult to converge for the core transition. Therefore, for the generalized length representation, the dyall.ae4z basis set suffices to properly describe high-order multipoles, although the linear dependence

TABLE III. Anisotropic oscillator oscillator strengths ($\frac{c}{\omega}\mathbf{k} = \mathbf{e}_z; \epsilon = \mathbf{e}_y$) of the $ns_{1/2} \rightarrow 7p_{1/2}$ $(n = 1, 7)$ transitions for the full semi-classical interaction operator and the dipole-length and velocity oscillator strengths, calculated with ground state orbitals and no restrictions on the space of virtual orbitals, within the multipolar gauge (lr: length representation) and Coulomb gauge (vr: velocity representation), computed at the 4c-TD-HF level of theory with different basis sets. Numbers in parentheses are exponents of 10.

Basis	ΔE (eV)	f_{full}	$f_{\text{lr}}^{(\rightarrow 0)}$	$f_{\text{vr}}^{(\rightarrow 0)}$	ratio (lr:vr)
		$7s_{1/2} \rightarrow 7p_{1/2}$			
dyall.ae2z	0.392	1.068(-3)	1.004(-3)	1.068(-3)	0.940
dyall.ae3z	0.383	1.012(-3)	9.686(-4)	1.012(-3)	0.957
dyall.ae4z	0.383	9.750(-4)	9.652(-4)	9.749(-4)	0.990
		$1s_{1/2} \rightarrow 7p_{1/2}$			
dyall.ae2z	104645.540	6.850(-5)	5.900(-5)	5.873(-5)	1.005
dyall.ae3z	104645.510	6.852(-5)	5.900(-5)	5.874(-5)	1.004
dyall.ae4z	104645.509	6.854(-5)	5.901(-5)	5.876(-5)	1.004

threshold needs to be adjusted.

From all types of multipoles, the velocity representation electric multipoles appear to be most problematic to converge. Even though the valence multipoles converge towards the numerical reference, the core multipoles contain deviations from the reference in the form of oscillations and additional peaks. Due to these artifacts, the basis set convergence seems to be inverted: larger basis sets deviate further from the reference. This suggests that the generalized velocity representation should be applied with caution for $n > 3$. For the generalized velocity representation, we recommend to use the dyall.ae3z basis set, which does not seem to suffer as much from the artifacts as the dyall.ae4z basis set. In addition, we recommend to not go further than $n = 3$, because after this order, the reliability of this scheme becomes questionable.

The full interaction operator does not suffer from these problems and is already converged with the dyall.ae2z basis. Considering that the truncated interaction also suffers from slow convergence with respect to the multipole expansion, we recommend to apply the full interaction when calculating X-ray transitions. This is the main message of this paper.

Our findings are transferable to the non-relativistic limit, because in this limit, the full interaction and the length representation electric multipole have the same characteristics.

Furthermore, the magnetic multipoles and velocity representation electric multipoles converge faster towards the numerical reference than equivalent 4c calculations, because the problems associated with linear dependence disappear upon taking this limit. Therefore, we expect that in the non-relativistic limit, the basis set requirements of multipole moments are less demanding.

Conclusions are possibly less obvious for the intermediate 2-component relativistic level. Our present approach would formally require the generation of radial distributions using properly picture-changed interaction operators, and these are for instance not available for the eXact 2-Component Hamiltonian (X2C), for which in general only a matrix representation, and not a real-space one, is available (see for instance discussion in Ref. 64). However, again the elimination of the small components suggests that basis set convergence should improve.

ACKNOWLEDGMENTS

N.H.L. acknowledges start-up funding from the School of Engineering Sciences in Chemistry, Biotechnology and Health (CBH), KTH Royal Institute of Technology. M.v.H. acknowledges funding from the French Ministry of Higher Education and Research. This work was performed using HPC resources from CALMIP (Calcul en Midi-Pyrenées; project P13154) and SNIC (Swedish National Infrastructure for Computing; SNIC 2022/5-220) at National Supercomputer Centre (NSC). We would like to thank Andreas Görling (Erlangen) and Frank Jensen (Aarhus) for valuable discussions.

SUPPLEMENTARY MATERIAL

Transition moments from CI and SCF linear response-theory. Conversion of the electric-length and electric-velocity multipoles at the TD-HF level of theory. Radial distributions with augmented basis sets and an analysis of the linear dependence issues of the small component function.

DATA AVAILABILITY STATEMENT

The data that support the findings of this study are openly available in ZENODO at https://doi.org/10.5281/zenodo.7885248, see also Ref. 65.

REFERENCES

[1] J. Als-Nielsen and D. McMorrow, *Elements of modern X-ray physics*, 2nd ed. (John Wiley & Sons, 2011) pp. 29–66.

[2] C. D. Rankine and T. J. Penfold, The Journal of Physical Chemistry A **125**, 4276 (2021).

[3] A. Bianconi, Applications of Surface Science **6**, 392 (1980).

[4] R. Stumm von Bordwehr, Annales de Physique **14**, 377 (1989).

[5] Y. Joly and S. Grenier, "Theory of X-Ray Absorption Near Edge Structure," in *X-Ray Absorption and X-Ray Emission Spectroscopy* (John Wiley & Sons, Ltd, 2016) Chap. 4, pp. 73–97.

[6] P. Pyykkö, Chemical Reviews **88**, 563 (1988).

[7] T. Fransson, S. Coriani, O. Christiansen, and P. Norman, The Journal of Chemical Physics **138**, 124311 (2013).

[8] K. Siegbahn, Reviews of Modern Physics **54**, 709 (1982).

[9] M. Drescher, M. Hentschel, R. Kienberger, M. Uiberacker, V. Yakovlev, A. Scrinzi, T. Westerwalbesloh, U. Kleineberg, U. Heinzmann, and F. Krausz, Nature **419**, 803 (2002).

[10] R. E. Stanton and S. Havriliak, The Journal of chemical physics **81**, 1910 (1984).

[11] K. G. Dyall and K. Fægri, Theoretica chimica acta **94**, 39 (1996).

[12] K. Fægri Jr and K. G. Dyall, in *Theoretical and Computational Chemistry*, Vol. 11 (Elsevier, 2002) pp. 259–290.

[13] M. A. Ambroise and F. Jensen, Journal of chemical theory and computation **15**, 325 (2018).

[14] M. A. Ambroise, A. Dreuw, and F. Jensen, Journal of Chemical Theory and Computation **17**, 2832 (2021).

[15] M. W. D. Hanson-Heine, M. W. George, and N. A. Besley, Chemical Physics Letters **699**, 279 (2018).

[16] G. Cavigliasso and D. P. Chong, The Journal of chemical physics **111**, 9485 (1999).

[17] J. Qian, E. J. Crumlin, and D. Prendergast, Physical Chemistry Chemical Physics **24**, 2243 (2022).

[18] L. K. Sørensen, M. Guo, R. Lindh, and M. Lundberg, Molecular Physics **115**, 174 (2017).

[19] L. K. Sørensen, E. Kieri, S. Srivastav, M. Lundberg, and R. Lindh, Physical Review A **99**, 013419 (2019).

[20]N. H. List, J. Kauczor, T. Saue, H. J. Aa. Jensen, and P. Norman, The Journal of chemical physics **142**, 244111 (2015).

[21]N. H. List, T. Saue, and P. Norman, Molecular Physics **115**, 63 (2017), https://doi.org/10.1080/00268976.2016.1187773.

[22]N. H. List, T. R. L. Melin, M. van Horn, and T. Saue, The Journal of chemical physics **152**, 184110 (2020).

[23]M. van Horn, T. Saue, and N. H. List, The Journal of Chemical Physics **156**, 054113 (2022).

[24]S. Bernadotte, A. J. Atkins, and C. R. Jacob, The Journal of chemical physics **137**, 204106 (2012).

[25]N. O. Foglia, D. Maganas, and F. Neese, The Journal of Chemical Physics **157** (2022), 10.1063/5.0094709, 084120.

[26]F. Jensen, *Introduction to computational chemistry*, 2nd ed. (John wiley & sons, 2017) pp. 194–208.

[27]W. L. Jolly and D. N. Hendrickson, Journal of the American Chemical Society **92**, 1863 (1970).

[28]H. Ågren, C. Medina-Llanos, K. V. Mikkelsen, and H. J. Aa. Jensen, Chemical physics letters **153**, 322 (1988).

[29]J. C. Slater, Physical Review **36**, 57 (1930).

[30]D. P. Chong, Canadian journal of chemistry **73**, 79 (1995).

[31]P. Manninen and J. Vaara, Journal of computational chemistry **27**, 434 (2006).

[32]M. Pecul, K. Ruud, and T. Helgaker, Chemical physics letters **388**, 110 (2004).

[33]M. Šindelka and N. Moiseyev, Physical Review A **76**, 043844 (2007).

[34]M. Khamesian, I. F. Galván, M. G. Delcey, L. K. Sørensen, and R. Lindh, in *Annual Reports in Computational Chemistry*, Vol. 15 (Elsevier, 2019) pp. 39–76.

[35]R. J. S. Crossley, in *Advances in atomic and molecular physics*, Vol. 5 (Elsevier, 1969) pp. 237–296.

[36]T. Saue, R. Bast, A. S. P. Gomes, H. J. Aa. Jensen, L. Visscher, I. A. Aucar, R. Di Remigio, K. G. Dyall, E. Eliav, E. Fasshauer, *et al.*, The Journal of chemical physics **152**, 204104 (2020).

[37]K. G. Dyall, I. P. Grant, C. T. Johnson, F. A. Parpia, and E. P. Plummer, Computer Physics Communications **55**, 425 (1989).

[38]R. A. Harris, The Journal of Chemical Physics **50**, 3947 (1969).

[39]A. F. Starace, Phys. Rev. A **3**, 1242 (1971).

[40]J. Linderberg and Y. Öhrn, *Propagators in quantum chemistry*, 2nd ed. (John Wiley & Sons, 2004) pp. 86–88.

[41]F. Furche, The Journal of Chemical Physics **114**, 5982 (2001).

[42]J. Olsen and P. Jørgensen, The Journal of chemical physics **82**, 3235 (1985).

[43]J. Oddershede, P. Jørgensen, and D. L. Yeager, Computer Physics Reports **2**, 33 (1984).

[44]R. Bast, H. J. Aa. Jensen, and T. Saue, International Journal of Quantum Chemistry **109**, 2091 (2009).

[45]I. P. Grant, *Relativistic quantum theory of atoms and molecules: theory and computation* (Springer, 2007) pp. 3–17.

[46]C. Froese-Fischer, T. Brage, and P. Johnsson, *Computational atomic structure: an MCHF approach* (CRC press, 1997) pp. 5–6.

[47]M. E. Rose, *Relativistic Electron Theory* (John Wiley & sons, 1961) pp. 163–169.

[48]P. Strange, *Relativistic Quantum Mechanics: with applications in condensed matter and atomic physics* (Cambridge University Press, 1998) pp. 243–248.

[49]T. H. Dunning and V. McKoy, J. Chem. Phys. **47**, 1735 (1967).

[50]F. W. Olver, D. W. Lozier, R. F. Boisvert, and C. W. Clark, *NIST handbook of mathematical functions hardback and CD-ROM* (Cambridge university press, 2010) pp. 262–267.

[51]DIRAC, a relativistic ab initio electronic structure program, Release DIRAC22 (2022), written by H. J. Aa. Jensen, R. Bast, A. S. P. Gomes, T. Saue and L. Visscher, with contributions from I. A. Aucar, V. Bakken, C. Chibueze, J. Creutzberg, K. G. Dyall, S. Dubillard, U. Ekström, E. Eliav, T. Enevoldsen, E. Faßhauer, T. Fleig, O. Fossgaard, L. Halbert, E. D. Hedegård, T. Helgaker, B. Helmich–Paris, J. Henriksson, M. van Horn, M. Iliaš, Ch. R. Jacob, S. Knecht, S. Komorovský, O. Kullie, J. K. Lærdahl, C. V. Larsen, Y. S. Lee, N. H. List, H. S. Nataraj, M. K. Nayak, P. Norman, G. Olejniczak, J. Olsen, J. M. H. Olsen, A. Papadopoulos, Y. C. Park, J. K. Pedersen, M. Pernpointner, J. V. Pototschnig, R. di Remigio, M. Repisky, K. Ruud, P. Sałek, B. Schimmelpfennig, B. Senjean, A. Shee, J. Sikkema, A. Sunaga, A. J. Thorvaldsen, J. Thyssen, J. van Stralen, M. L. Vidal, S. Villaume, O. Visser, T. Winther, S. Yamamoto and X. Yuan (available at http://dx.doi.org/10.5281/zenodo.6010450, see also http://www.diracprogram.org).

[52] J. Thyssen, *Development and Applications of Methods for Correlated Relativistic Calculations of Molecular Properties*, Ph.D. thesis, University of Southern Denmark (2001), Available from http://dirac.chem.sdu.dk/thesis/thesis-jth2001.pdf.

[53] H. Lefebvre-Brion, "CECAM-ORSAY Documentation for Molecular Calculations – 1970," (2021).

[54] P. S. Bagus and H. F. Schaefer III, The Journal of Chemical Physics **55**, 1474 (1971), This paper employs overlap selection, but does not write it explicitly. The proper keyword MOORDR is found on page 9 of Ref. 53.

[55] A. T. B. Gilbert, N. A. Besley, and P. M. W. Gill, The Journal of Physical Chemistry A **112**, 13164 (2008).

[56] M. Stener, G. Fronzoni, and M. de Simone, Chemical physics letters **373**, 115 (2003).

[57] C. South, A. Shee, D. Mukherjee, A. K. Wilson, and T. Saue, Physical Chemistry Chemical Physics **18**, 21010 (2016).

[58] T. Saue and H. J. Aa. Jensen, The Journal of chemical physics **111**, 6211 (1999).

[59] K. G. Dyall, The Journal of Physical Chemistry A **113**, 12638 (2009), The basis sets are available from Ref. 60.

[60] K. G. Dyall, "Dyall double-zeta, triple-zeta, and quadruple-zeta basis set archive files," (2023).

[61] I. P. Grant, Physical Review A **25**, 1230 (1982).

[62] W. H. E. Schwarz and H. Wallmeier, Molecular Physics **46**, 1045 (1982).

[63] K. G. Dyall and K. Fægri Jr, Chemical physics letters **174**, 25 (1990).

[64] T. Saue, ChemPhysChem **12**, 3077 (2011).

[65] M. van Horn, N. H. List and T. Saue, "Replication Data for: Transition Moments Beyond the Electric-Dipole Approximation: Visualization and Basis Set Requirements," (2023).